

Effects of a subadiabatic layer on convection and dynamos in spherical wedge simulations

P. J. KÄPYLÄ^{a,b,c,d}, M. VIVIANI^c, M. J. KÄPYLÄ^{c,b}, and A. BRANDENBURG^{d,e,f,g}

^aLeibniz-Institut für Astrophysik, An der Sternwarte 16, D-14482 Potsdam, Germany

^bReSoLVE Centre of Excellence, Department of Computer Science, P.O. Box 15400, FI-00076 Aalto, Finland

^cMax-Planck-Institut für Sonnensystemforschung, Justus-von-Liebig-Weg 3, D-37077 Göttingen, Germany

^dNORDITA, KTH Royal Institute of Technology and Stockholm University, Roslagstullsbacken 23, SE-10691 Stockholm, Sweden

^eDepartment of Astronomy, AlbaNova University Center, Stockholm University, SE-10691 Stockholm, Sweden

^fJILA and Department of Astrophysical and Planetary Sciences, Box 440, University of Colorado, Boulder, CO 80303, USA

^gLaboratory for Atmospheric and Space Physics, 3665 Discovery Drive, Boulder, CO 80303, USA

(April 15, 2022, Revision: 1.93)

We consider the effect of a subadiabatic layer at the base of the convection zone on convection itself and the associated large-scale dynamos in spherical wedge geometry. We use a heat conduction prescription based on the Kramers opacity law which allows the depth of the convection zone to dynamically adapt to changes in the physical characteristics such as rotation rate and magnetic fields. We find that the convective heat transport is strongly concentrated toward the equatorial and polar regions in the cases without a substantial radiative layer below the convection zone. The presence of a stable layer below the convection zone significantly reduces the anisotropy of radial enthalpy transport. Furthermore, the dynamo solutions are sensitive to subtle changes in the convection zone structure. We find that the kinetic helicity changes sign in the deeper parts of the convection zone at high latitudes in all runs. This region expands progressively toward the equator in runs with a thicker stably stratified layer.

Keywords: convection, turbulence, dynamos, magnetohydrodynamics

1. Introduction

Both differential rotation and dynamo action in late-type stars such as the Sun are driven by the interaction of turbulent convection and global rotation of the stars (e.g. [Miesch and Toomre 2009](#), [Brun and Browning 2017](#)). While a popular class of mean-field dynamos, known as the flux transport dynamos (e.g. [Dikpati and Charbonneau 1999](#)), rely on processes in the boundary layers at the base and near the surface of the convection zone (CZ), large-eddy simulations of stellar convection have demonstrated that solar-like magnetic activity can be obtained without the inclusion of such layers (e.g. [Ghizaru *et al.* 2010](#), [Käpylä *et al.* 2012](#), [Warnecke *et al.* 2014](#), [Passos and Charbonneau 2014](#), [Augustson *et al.* 2015](#), [Käpylä *et al.* 2016](#)). However, this does not necessarily imply that the solar dynamo works like the simulations suggest, because they face problems of their own. Numerical simulations appear

*Corresponding author. Email: pkapyla@aip.de

to produce much higher velocity amplitudes at large horizontal scales in comparison to what is found with helioseismic inversions (Hanasoge *et al.* 2012, Gizon and Birch 2012).

There is another piece of evidence that also suggests that the velocities are too high in simulations. This evidence comes from simulations that adopt the solar luminosity and rotation rate: instead of a solar-like differential rotation profile with fast equator and slow poles, an antisolar one with slow equator and fast poles is obtained. This is indicative of a lower rotational influence on the flow in simulations in comparison to the Sun (e.g. Gastine *et al.* 2014, Käpylä *et al.* 2014, Hotta *et al.* 2015). This discrepancy between observations and simulations has been named the “convective conundrum” (O’Mara *et al.* 2016). Furthermore, the simulated rotation profiles are nearly in Taylor-Proudman balance, corresponding to cylindrical isocontours of constant angular velocity (e.g. Brun and Toomre 2002, Miesch *et al.* 2006, Käpylä *et al.* 2011a) in comparison to more spoke-like isocontours inferred for the Sun (Schou *et al.* 1998).

A possible remedy to the Taylor-Proudman dilemma is to assume that the lower part of the CZ is slightly subadiabatic (Rempel 2005), in which case a thermal wind produced by the negative entropy fluctuations leads to a more conical angular velocity profile (Miesch *et al.* 2006). A related idea has been invoked to crack the convective conundrum: if convection is driven only in the near-surface layers by radiative cooling (Spruit 1997, Brandenburg 2016), the larger-scale convective modes such as giant cells are not excited, leading to a reduction of power at large horizontal scales (e.g. Cossette and Rast 2016). In this scenario the bulk of the revised CZ is being mixed due to overshooting by downflow plumes originating near the surface.

Recent numerical simulations indeed suggest that convection is driven by cooling near the surface (Cossette and Rast 2016, Käpylä *et al.* 2017b) and that the lower part of the convection zone is weakly subadiabatic (e.g. Käpylä *et al.* 2017b, Hotta 2017, Bekki *et al.* 2017, Karak *et al.* 2018). Evidence of a changing structure of convection from a tree-like (decreasing number of downflow plumes with increasing depth) to a forest-like structure (constant number of plumes) has also been reported (Käpylä *et al.* 2017b). Although the extent of the subadiabatic region is at most roughly 40 per cent of the combined depth of the convection and overshoot zones (Hotta 2017). In a subsequent study, Karak *et al.* (2018) found a similar effect in non-rotating hydrodynamic convection simulations at thermal Prandtl numbers above unity. However, the effect was significantly weaker in simulations including rotation. The main difference of the present study as opposed to that of Karak *et al.* (2018) is that we also include setups where overshoot and radiative layers are present, and investigate cases where dynamo action occurs.

Large-scale dynamos in stellar convective envelopes can also be affected by a subadiabatic layer at the base of the convection zone: such a layer can store magnetic flux (e.g. Browning *et al.* 2006) and it can possibly contribute to inverting the kinetic helicity of the flow in the deep parts of the CZ (Duarte *et al.* 2016). Such inversion is a possible way out of the ‘modern dynamo dilemma’ that plagues current simulators: the equatorward migrating dynamo waves are most likely due to a region of negative radial shear within the CZ, which is not present in the Sun (Warnecke *et al.* 2014). This is a variation of Parker’s dynamo dilemma (Parker 1987) where the observed differential rotation profile and theoretically expected sign of kinetic helicity lead to poleward migration of activity belts (see also Deluca and Gilman 1986).

In the current study we present first results from convection-driven dynamo simulations in spherical wedges where stably stratified layers are present with a setup that is similar to that of the hydrodynamic Cartesian runs of Käpylä *et al.* (2017b), where a physics-based rather than a prescribed formulation for the heat conduction was used.

2. Model

Our simulation setup is similar to that used earlier (Käpylä *et al.* 2013, 2016, 2017a). However, the current models differ in a few key aspects from the previous studies. We solve the equations of fully compressible magnetohydrodynamics

$$\frac{\partial \mathbf{A}}{\partial t} = \mathbf{U} \times \mathbf{B} - \eta \mu_0 \mathbf{J}, \quad (1)$$

$$\frac{D \ln \rho}{Dt} = -\nabla \cdot \mathbf{U}, \quad (2)$$

$$\frac{D\mathbf{U}}{Dt} = \mathbf{g} - 2\boldsymbol{\Omega}_0 \times \mathbf{U} - \frac{1}{\rho}(\nabla p + \mathbf{J} \times \mathbf{B} + \nabla \cdot 2\nu \rho \mathbf{S}), \quad (3)$$

$$T \frac{Ds}{Dt} = \frac{1}{\rho} \left[\eta \mu_0 \mathbf{J}^2 - \nabla \cdot (\mathbf{F}^{\text{rad}} + \mathbf{F}^{\text{SGS}}) - \Gamma_{\text{cool}} \right] + 2\nu \mathbf{S}^2, \quad (4)$$

where \mathbf{A} is the magnetic vector potential, \mathbf{U} is the velocity, $\mathbf{B} = \nabla \times \mathbf{A}$ is the magnetic field, η is the magnetic diffusivity, μ_0 is the permeability of vacuum, $\mathbf{J} = \nabla \times \mathbf{B} / \mu_0$ is the current density, $D/Dt = \partial/\partial t + \mathbf{U} \cdot \nabla$ is the advective time derivative, ρ is the density, $\mathbf{g} = -GM_\odot \hat{\mathbf{r}}/r^2$ is the acceleration due to gravity, where $G = 6.67 \cdot 10^{-11} \text{ N m}^2 \text{ kg}^{-2}$ is the universal gravitational constant, and $M_\odot = 2.0 \cdot 10^{30} \text{ kg}$ is the solar mass, $\boldsymbol{\Omega}_0 = (\cos \theta, -\sin \theta, 0)\Omega_0$ is the angular velocity vector, where Ω_0 is the rotation rate of the frame of reference, ν is the kinematic viscosity, p is the pressure, and s is the specific entropy with $Ds = c_V D \ln p - c_P D \ln \rho$, where c_V and c_P are the specific heats in constant volume and pressure, respectively. The gas is assumed to obey the ideal gas law, $p = \mathcal{R} \rho T$, where $\mathcal{R} = c_P - c_V$ is the gas constant. The rate of strain tensor is given by

$$S_{ij} = \frac{1}{2}(U_{i;j} + U_{j;i}) - \frac{1}{3}\delta_{ij} \nabla \cdot \mathbf{U}, \quad (5)$$

where the semicolons refer to covariant derivatives (Mitra *et al.* 2009). The radiative flux is given by

$$\mathbf{F}^{\text{rad}} = -K \nabla T, \quad (6)$$

where $K = c_P \rho \chi$ is the heat conductivity, which is allowed to vary in a dynamic and local fashion. We use two heat conduction schemes, where K is either a fixed function of height $K = K(r)$ or it depends on density and temperature $K = K(\rho, T)$. In the former case we use the same profile as defined in Käpylä *et al.* (2013). In the latter case K is computed from

$$K = \frac{16\sigma_{\text{SB}} T^3}{3\kappa \rho}, \quad (7)$$

where σ_{SB} is the Stefan-Boltzmann constant and κ is the opacity. The latter is assumed to obey a power law

$$\kappa = \kappa_0 (\rho/\rho_0)^a (T/T_0)^b, \quad (8)$$

where ρ_0 and T_0 are reference values of density and temperature. Combining Equations (7) and (8) gives (Barekat and Brandenburg 2014)

$$K(\rho, T) = K_0 (\rho/\rho_0)^{-(a+1)} (T/T_0)^{3-b}. \quad (9)$$

In the current study we use the combination $a = 1$ and $b = -7/2$, which corresponds to the Kramers opacity law for free-free and bound-free transitions (Weiss *et al.* 2004). This scheme has previously been used in local simulations of convection (Brandenburg *et al.* 2000, Käpylä *et al.* 2017b).

The subgrid scale (SGS) flux is given by

$$\mathbf{F}^{\text{SGS}} = -\chi_{\text{SGS}}\rho T \nabla s', \quad (10)$$

where χ_{SGS} is the (constant) SGS diffusion coefficient for the entropy fluctuation $s' = s - \langle s \rangle_{\theta\phi}$, where $\langle s \rangle_{\theta\phi}$ is the horizontally averaged or spherically symmetric part of the specific entropy.

The last term on the rhs of Equation (4) models the cooling near the surface of the star:

$$\Gamma_{\text{cool}} = -\Gamma_0 f(r) (T_{\text{cool}} - \langle T \rangle_{\theta\phi}), \quad (11)$$

where Γ_0 is a cooling luminosity, $\langle T \rangle_{\theta\phi}$ is the horizontally averaged temperature, and $T_{\text{cool}} = T_{\text{cool}}(r)$ is a radius-dependent cooling temperature coinciding with the initial stratification. In our previous studies (Käpylä *et al.* 2010, 2011b) we fixed the temperature to a constant at the outer radial boundary. The main effect of the changed boundary condition is that no isothermal and strongly subadiabatic layer forms near the surface.

2.1. System parameters and diagnostics quantities

The wedges used in the current simulations span $r_{\text{in}} < r < R_{\odot}$ in radius, where $r_{\text{in}} = 0.7R_{\odot}$ and $R_{\odot} = 7 \cdot 10^8$ m is the solar radius, $15^\circ < \theta < 165^\circ$ in colatitude, and $0 < \phi < 90^\circ$ in longitude. Our simulations are defined by the energy flux imposed at the bottom boundary, $F_b = -(K\partial T/\partial r)|_{r=r_{\text{in}}}$, the values of K_0 , a , b , ρ_0 , T_0 , Ω_0 , ν , η , χ_{SGS} , and the fixed profile of K in cases where the Kramers opacity law is not used. Furthermore, the radial profile of $f(r)$ is piecewise constant with $f(r) = 0$ in $r_{\text{in}} < r < 0.98R_{\odot}$, and smoothly connecting to $f(r) = 1$ above $r = 0.98R_{\odot}$. We use a significantly higher luminosity than in the Sun to avoid the time step being limited by sound waves. $L_{\text{ratio}} = L_0/L_{\odot}$, where L_0 is the luminosity of the simulation and $L_{\odot} = 3.83 \cdot 10^{26}$ W is the corresponding solar value, quantifies the luminosity ratio. The non-dimensional luminosity is given by

$$\mathcal{L} = \frac{L_0}{\rho_0(GM_{\odot})^{3/2}R_{\odot}^{1/2}}. \quad (12)$$

The initial stratification is determined by the non-dimensional pressure scale height at the surface

$$\xi_0 = \frac{\mathcal{R}T_1}{GM_{\odot}/R_{\odot}}, \quad (13)$$

where T_1 is the temperature at the surface ($r = R_{\odot}$).

The relations between viscosity, magnetic diffusivity, and SGS diffusion are given by the Prandtl numbers

$$\text{Pr}_{\text{SGS}} = \frac{\nu}{\chi_{\text{SGS}}}, \quad \text{Pm} = \frac{\nu}{\eta}. \quad (14)$$

We use $\text{Pr}_{\text{SGS}} = \text{Pm} = 1$ in all of our runs. The Prandtl number related with the radiative conductivity,

$$\text{Pr} = \frac{\nu}{\chi}, \quad (15)$$

where $\chi = K/c_P\rho$ is the radiative diffusivity varies as a function of radius and time. The efficiency of convection is quantified by the Rayleigh number

$$\text{Ra} = \frac{GM_{\odot}(\Delta r)^4}{\nu\chi_{\text{SGS}}R_{\odot}^2} \left(-\frac{1}{c_P} \frac{ds_{\text{hs}}}{dr} \right)_{r_m}, \quad (16)$$

where $\Delta r = 0.3R_{\odot}$ is the depth of the layer, s_{hs} is the entropy in a one-dimensional non-convecting hydrostatic model, evaluated at the middle of the domain at $r_m = 0.85R_{\odot}$. We

note that in the cases with a Kramers-based heat conduction prescription, only a very thin surface layer is convectively unstable, see, e.g., Fig. 7 of [Brandenburg \(2016\)](#), such that $Ra < 0$ at $r = r_m$. We additionally quote the initial value of the Nusselt number (e.g. [Hurlburt et al. 1984](#), [Brandenburg 2016](#)):

$$Nu = \frac{\nabla_{\text{rad}}}{\nabla_{\text{ad}}}, \quad (17)$$

just below the cooling layer at $r = 0.98R_\odot$ where

$$\nabla_{\text{rad}} = \frac{\mathcal{R}}{Kg} F_{\text{tot}}, \quad \text{and} \quad \nabla_{\text{ad}} = 1 - \frac{1}{\gamma}, \quad (18)$$

are the radiative and adiabatic temperature gradients, and where $g = |\mathbf{g}|$, and $F_{\text{tot}} = L_0/(4\pi r^2)$. The effect of rotation is controlled by the Taylor number

$$Ta = (2\Omega_0 \Delta r^2 / \nu^2)^2. \quad (19)$$

The fluid and magnetic Reynolds numbers are

$$Re = \frac{u_{\text{rms}}}{\nu k_f} \quad \text{and} \quad Re_M = \frac{u_{\text{rms}}}{\eta k_f}, \quad (20)$$

respectively, where $k_f = 2\pi/\Delta r \approx 21/R_\odot$ is used as an estimate of the radial extent of convection cells.

The rotational influence on the flow is quantified by the Coriolis number

$$Co = \frac{2\Omega_0}{u_{\text{rms}} k_f}. \quad (21)$$

Mean quantities refer either to azimuthal (denoted by an overbar) or horizontal averages (denoted by angle brackets with subscript $\theta\phi$). Additional time averaging is also performed unless stated otherwise.

2.2. Initial and boundary conditions

The initial stratification is polytropic with $n = 1.5$ corresponding to an isentropic stratification. We use $\xi_0 = 0.01$ which results in an initial density contrast of roughly 60. In cases with a fixed heat conductivity profile, the value of K at $r = r_{\text{in}}$ is set such that the flux through the boundary is $L_0/4\pi r_{\text{in}}^2$. The flux at the outer radius, however, is much lower and the convective instability arises from the fact that the system is not in thermodynamic equilibrium driven by the efficient surface cooling (see e.g. [Käpylä et al. 2013](#)). In the cases with Kramers heat conductivity, the value of K at the bottom of the domain is varied by changing the value of K_0 in Eq. (9) to probe the influence it has on the depth of the convection zone. In the fiducial case, a nominal value K_0^{nom} is computed such that $F_{\text{rad}} = F_{\text{tot}}$ at the bottom of the domain. We probe a set of runs where the value of $\tilde{K}_0 = K_0/K_0^{\text{nom}}$ is increased. These runs correspond to more efficient radiative diffusion for a given thermal stratification. The expectation is that this leads to the formation of a stably stratified radiative layer at the bottom of the domain.

The radial and latitudinal boundaries are assumed impenetrable and stress-free for the flow. On the bottom boundary, a fixed heat flux is prescribed. On the outer and the latitudinal boundaries, the gradients of thermodynamic quantities are set to zero; see [Käpylä et al. \(2013\)](#). For the magnetic field we apply a vertical field condition at the upper, and a perfect conductor condition at the lower boundary. On the latitudinal boundaries the field is assumed

Table 1. Summary of the runs. All runs have $L_{\text{ratio}} = 2.1 \cdot 10^5$, $\Omega = 3\Omega_{\odot}$, $\text{Pr}_{\text{SGS}} = \text{Pr}_{\text{M}} = 1$, $\nu = 1.46 \cdot 10^8 \text{ m}^2 \text{ s}^{-1}$, $\text{Ta} = 2.33 \cdot 10^7$, $\xi_0 = 0.01$, and grid resolution $144 \times 288 \times 144$.

Run	Ra [10^7]	Nu	Nu _{sat}	Re	Co	r_{BZ}	r_{DZ}	r_{OZ}	d_{BZ}	d_{DZ}	d_{OZ}	Δt [yr]	K	\tilde{K}_0
HDp	3.0	156	156	37	0.0	(0.76	0.70	0.70	0.24	0.06	0.00)	35	profile	–
HD1	-	3167	2599	34	0.0	(0.76	0.71	0.70	0.24	0.06	0.01)	10	Kramers	1.0
HD2	-	1843	1524	32	0.0	(0.79	0.73	0.70	0.21	0.07	0.03)	10	Kramers	1.7
HD3	-	972	786	30	0.0	0.82	0.77	0.71	0.18	0.06	0.06)	12	Kramers	3.2
HD4	-	590	440	29	0.0	0.85	0.80	0.73	0.15	0.05	0.07)	11	Kramers	5.4
RHDp	3.0	156	156	29	4.1	(0.75	0.70	0.70	0.25	0.05	0.00)	49	profile	–
RHD1	-	3167	3034	32	3.8	(0.75	0.70	0.70	0.25	0.05	0.00)	29	Kramers	1.0
RHD2	-	1843	1772	30	4.0	(0.78	0.74	0.71	0.22	0.04	0.03)	27	Kramers	1.7
RHD3	-	972	882	29	4.2	0.79	0.78	0.72	0.21	0.01	0.06)	29	Kramers	3.2
RHD4	-	590	479	27	4.4	0.82	0.81	0.76	0.18	0.01	0.05)	22	Kramers	5.4
MHDp	3.0	156	156	29	4.2	(0.76	0.70	0.70	0.24	0.06	0.00)	44	profile	–
MHD1	-	3167	3004	32	3.8	(0.76	0.70	0.70	0.24	0.06	0.00)	63	Kramers	1.0
MHD2	-	1843	1743	29	4.1	(0.78	0.74	0.71	0.22	0.05	0.03)	74	Kramers	1.7
MHD3	-	972	868	26	4.6	0.80	0.78	0.72	0.20	0.02	0.06)	64	Kramers	3.2
MHD4	-	590	473	25	4.8	0.82	0.81	0.77	0.18	0.01	0.04)	72	Kramers	5.4

The values for runs RHDp, RHD1, RHD2, MHDp, MHD1, and MHD2, where strong latitudinal variations are seen, are listed in parentheses and should be considered as uncertain. Here the values of Nu refer to the initial state and Nu_{sat} to the saturated convective state.

to be tangential to the boundary. These conditions are given by:

$$\frac{\partial A_r}{\partial r} = 0, \quad \frac{\partial^2 A_\theta}{\partial r^2} = -2 \frac{\partial A_\theta}{\partial r}, \quad \frac{\partial^2 A_\phi}{\partial r^2} = -2 \frac{\partial A_\phi}{\partial r} \quad (r = r_0), \quad (22)$$

$$A_r = 0, \quad \frac{\partial A_\theta}{\partial r} = -\frac{A_\theta}{r}, \quad \frac{\partial A_\phi}{\partial r} = -\frac{A_\phi}{r} \quad (r = R_\odot), \quad (23)$$

$$A_r = \frac{\partial A_\theta}{\partial \theta} = A_\phi = 0 \quad (\theta = \theta_0, \pi - \theta_0). \quad (24)$$

Equation (22) differs from previously used conditions; see, e.g., Eq.(10) of Käpylä *et al.* (2013), where instead the tangential electric field was assumed to vanish on the boundary. The azimuthal direction is periodic for all quantities. The velocity and magnetic fields are initialized with random Gaussian noise fluctuations with amplitudes on the order of 0.1 m s^{-1} and 0.1 Gauss , respectively.

3. Results

We perform three sets of simulations denoted as HD, RHD, and MHD. In Set HD, we model non-rotating convection, where \tilde{K}_0 is varied to control the depth of the convection zone. The effect of increasing \tilde{K}_0 is to make radiative diffusion more efficient. This is particularly important in the deep parts of the domain where the temperature is high due to the strong temperature dependency of the heat conduction ($K \propto T^{6.5}$, see Equation (9)). Thus the expectation is that with higher values of \tilde{K}_0 , a radiative layer develops at the bottom of the domain. In the RHD runs, we take the HD runs and add rotation with $\Omega = 3\Omega_{\odot}$, where $\Omega_{\odot} = 2.7 \cdot 10^{-6} \text{ s}^{-1}$ is the mean solar rotation rate. In the MHD set, magnetic fields are added to the RHD setup to study the effects of stably stratified layers on the dynamo. A run with a fixed profile of K , denoted by a suffix “p”, is used as reference in each set with the same variation of physical ingredients. The runs are listed in Table 1.

The value of Ω_0 in the rotating simulations is chosen such that a solar-like differential rotation is obtained. The current setups with a Kramers-based heat conduction tend to produce anti-solar differential rotation at solar luminosity and rotation rate. Visualizations of the flow fields realized in representative runs without and with rotation are shown in Figure 1. The non-rotating cases qualitatively resemble mixing length ideas in that the horizontal scale of the

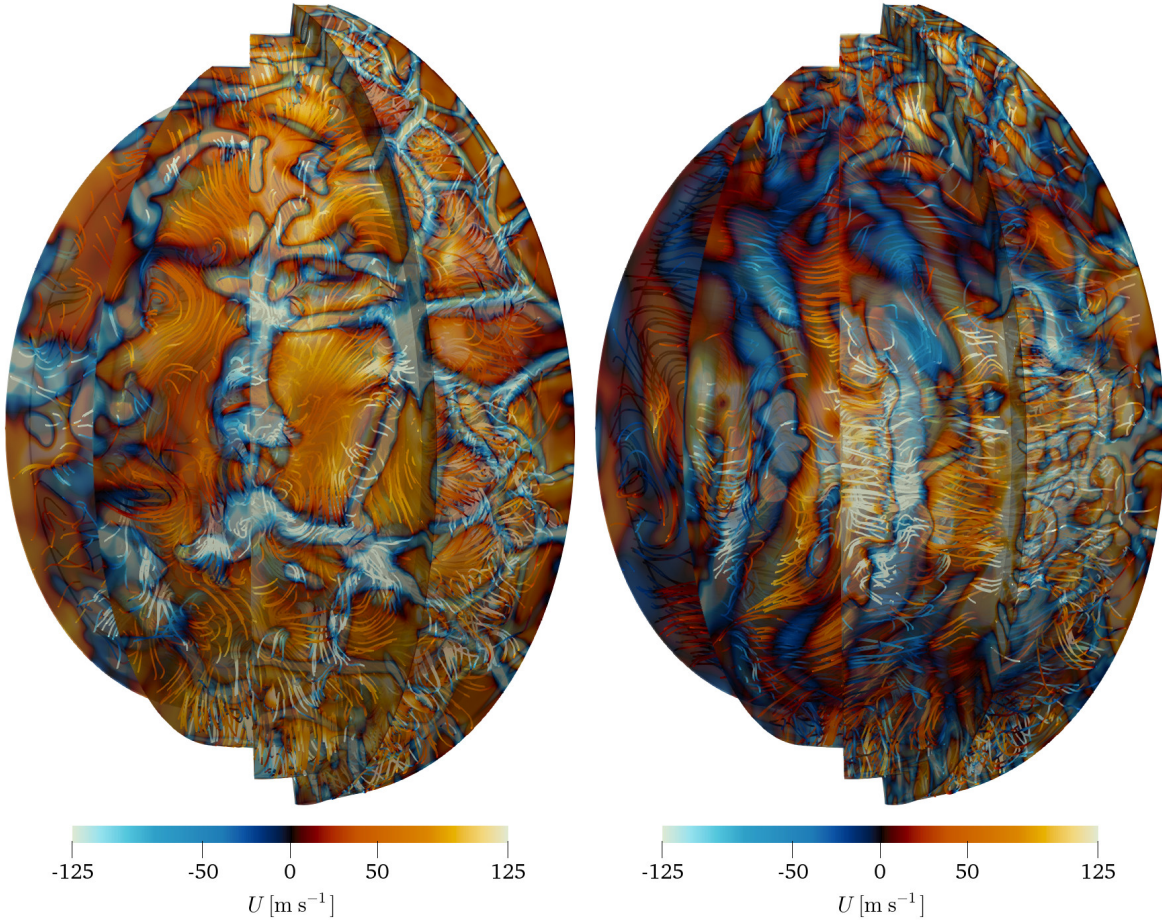


Figure 1. Streamlines of the total velocity and contours of vertical velocity at the periphery in snapshots of Runs HD1 (left) and MHD2 (right). The colour-coding of both is indicated at the bottom of each panel. The horizontal cuts from left to right are shown from depths $r/R_{\odot} = 0.78, 0.85, 0.92,$ and 0.99 .

convective eddies increases as a function of depth. The rotating cases are dominated by banana cells (e.g. [Busse 1970](#), [Gilman and Miller 1986](#)) in the equatorial regions and by small scale convection at high latitudes, and this carries over also to the magnetic cases. The convective scales show significantly less variation in depth in comparison to non-rotating convection.

3.1. Convective energy transport and structure of the convection zone

In an earlier study, [Käpylä *et al.* \(2017b\)](#) found that a stably stratified layer, where the enthalpy flux is nevertheless directed outward, develops at the bottom of the convection zone if a smoothly varying profile for the heat conduction is used. Furthermore, when the Kramers opacity law is applied, the depth of the convection zone is a result of the simulation rather than fixed a priori (see the values of r_{OZ} in [Table 1](#)). Here we extend these studies to more realistic spherical geometry and take into account global rotation and dynamo-generated magnetic fields.

The enthalpy flux is defined as

$$\overline{F}_i^{\text{enth}} = c_P \overline{(\rho u_i)' T'}, \quad (25)$$

where the primes denote fluctuation from the azimuthal mean denoted by an overbar. We use the same nomenclature as in [Käpylä *et al.* \(2017b\)](#) to distinguish the different layers in the

Table 2. Classification of zones.

Quantity/zone	Buoyancy (BZ)	Deardorff (DZ)	Overshoot (OZ)	Radiation (RZ)
$\overline{F}_r^{\text{enth}}$	> 0	> 0	< 0	≈ 0
$\nabla_r \bar{s}$	< 0	> 0	> 0	> 0

domain. This entails classifying the layers by the signs of the radial enthalpy flux $\overline{F}_r^{\text{enth}}$ and the radial gradient of entropy, $\nabla_r \bar{s} = \partial \bar{s} / \partial r$, see Table 2. The bottom of the buoyancy zone (BZ) is where $\nabla_r \bar{s}$ changes from negative to positive, whereas the bottom of the Deardorff zone (DZ) is where $\overline{F}_r^{\text{enth}}$ changes from positive to negative; see [Brandenburg \(2016\)](#) for an explanation of a contribution to $\overline{F}_r^{\text{enth}}$ by [Deardorff \(1966\)](#). Finally, the bottom of the overshoot zone (OZ) is where the $|\overline{F}_r^{\text{enth}}|$ falls below a threshold value, here chosen to be 2.5 per cent of the luminosity corresponding to the input flux. In the commonly accepted view the convection zone consists of the Schwarzschild-unstable layer and the Deardorff zone is absent (e.g. [Zahn 1991](#)). This coincides with the predictions from mixing length theory (e.g. [Vitense 1953](#)). In our revised view, the convection zone (CZ) is considered to encompass both the BZ and the DZ.

We show the time-averaged luminosity of the radial enthalpy flux, $L_r^{\text{enth}} = 4\pi r^2 \overline{F}_r^{\text{enth}}$ and the direction of vectorial enthalpy flux, $\overline{\mathbf{F}}^{\text{enth}} = (\overline{F}_r^{\text{enth}}, \overline{F}_\theta^{\text{enth}}, 0)$ in the meridional plane for a selection of runs in Figure 2. In the non-rotating, hydrodynamic run HD1, the enthalpy flux is directed radially outward and approximately uniformly distributed in latitude with the exception of regions in the immediate vicinity of the latitudinal boundaries where the enthalpy flux is enhanced. The differences between Runs HDp and HD1 are very minor in that both develop a DZ, covering roughly 20 per cent of the depth of the domain, at the base of the CZ. No appreciable overshoot region develops in either run. This is unsurprising because the heat conductivity in these models is chosen such that it just delivers the input flux through the boundary and decreases rapidly in the upper layers, necessitating convection to transport some fraction of the energy there. Increasing the value of \tilde{K}_0 (from Runs HD2 to HD4) enhances the radiative diffusion—in particular in the deep parts where the temperature is high. This leads gradually to the formation of a radiative zone (RZ) at the base of the domain; see Figure 2(c). In the non-rotating case it is meaningful to average over latitude and to obtain estimates of the depths of the different layers. These are listed as d_{BZ} , d_{DZ} , and d_{OZ} in Table 1. We note that only in Runs HD3 and HD4 the domain is deep enough to allow the formation of an RZ and that the depths of the DZ and/or OZ are thus underestimated for Runs HDp, HD1, and HD2. A similar argument applies to the runs presented by [Karak et al. \(2018\)](#) and [Bekki et al. \(2017\)](#). In Runs HD3 and HD4, the subadiabatic but mixed layers (DZ and OZ) cover 38 and 44 per cent of the total depth of the mixed zone. This is in good agreement with the results from local simulations (e.g. [Käpylä et al. 2017b](#), [Hotta 2017](#)).

This picture is radically altered in the rotating cases, see the lower panels of Figure 2. The most prominent new feature is the strong latitude dependence of the radial enthalpy flux: the energy transport is strongly concentrated toward high latitudes near the latitude boundaries and near the equator. A major difference between Runs MHDp and MHD1 is that in the former, the enthalpy flux is roughly equally efficient at high and low latitudes ($\Theta \gtrsim 55^\circ$ and $\Theta \lesssim 30^\circ$, where $\Theta = 90^\circ - \theta$ is the latitude), whereas in the latter the high latitude flux is suppressed. Another difference is that in Run MHDp the Deardorff layers at mid-latitudes ($20^\circ \lesssim \Theta \lesssim 35^\circ$) covers almost the whole depth of the domain whereas in Run MHD1 the latitude variation is less extreme although still substantial; see the solid black and white lines in Figure 2(d) and (e). Near the equator ($\Theta \lesssim 10^\circ$), the Deardorff layer is either very thin (MHDp) or missing completely (MHD1). A possible explanation to the

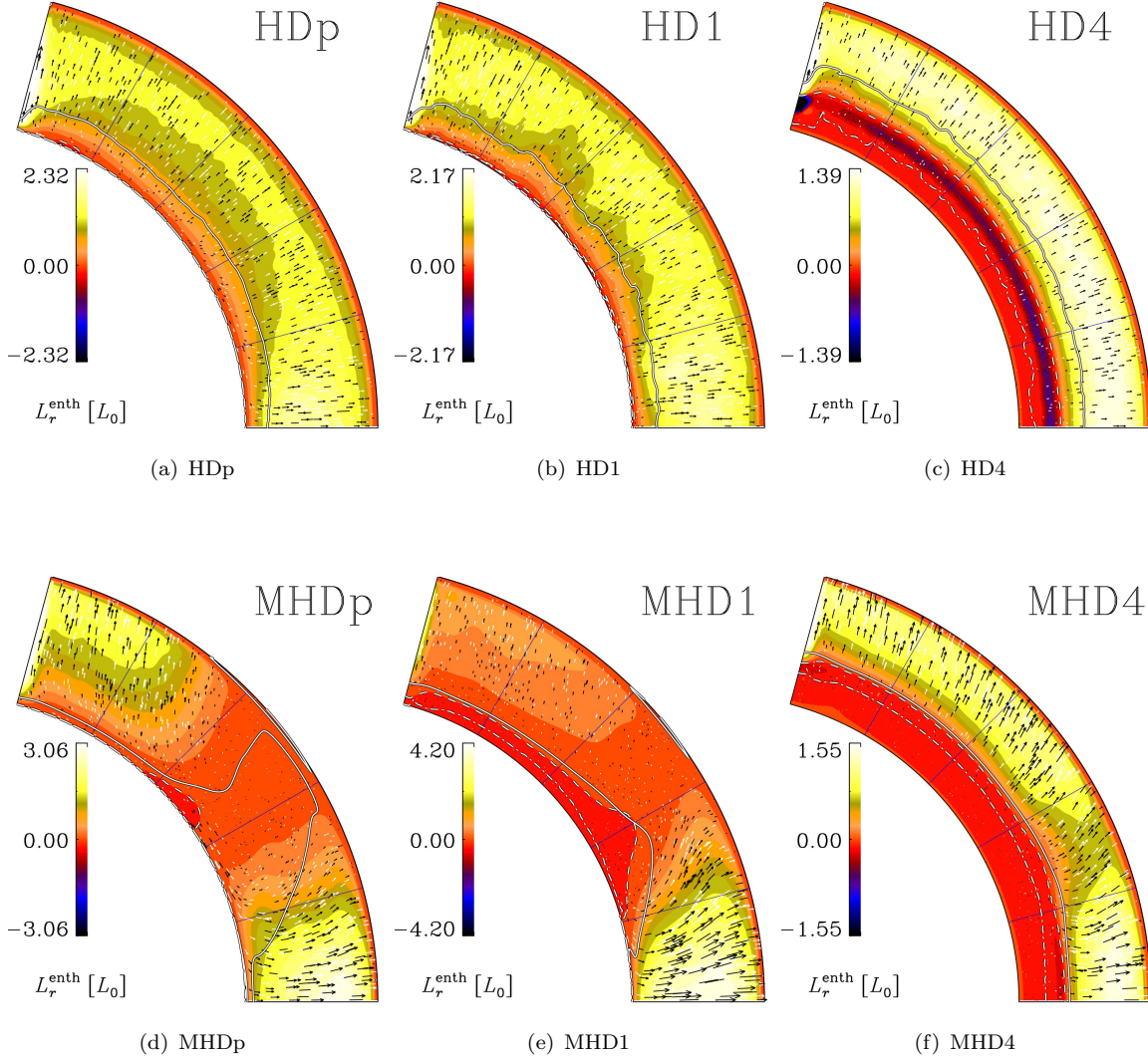


Figure 2. Color contours: time-averaged luminosity of the radial enthalpy flux normalized by the total luminosity from non-rotating, hydrodynamic runs HDp, HD1, and HD4 (top row) and rotating dynamo runs MHDp, MHD1, and MHD4 (lower row). The arrows indicate the magnitude and direction of the vectorial enthalpy flux, $\mathbf{F}^{\text{enth}} = (\overline{F}_r^{\text{enth}}, \overline{F}_\theta^{\text{enth}}, 0)$ in the meridional plane. The black and white solid, dashed, and dash-dotted lines indicate the bottoms of the buoyancy, Deardorff, and overshoot zones, respectively. The thin blue lines indicate latitudes 15, 30, 45, and 60 degrees.

very deep mid-latitude Deardorff layer in Run MHDp is that the current simulations are only moderately supercritical in terms of the Rayleigh number and that convection is harder to excite in the mid-latitude regions in rotating cases (e.g. Gilman 1977). This is exacerbated by the rigid combination of a fixed heat conductivity profile and a constant temperature boundary condition applied at the radial top boundary. The reason why the Deardorff zone is significantly shallower in Run MHD1 is because the heat conductivity adapts in response to changes in the thermal structure. Convectively stable mid-latitudes have been reported from similar simulation setups with fixed K -profile and surface temperature by (Käpylä *et al.* 2011b). However, in cases where, for example, a black body radiation condition is applied at the surface, the mid-latitudes remain convectively unstable and allow for significant latitudinal variation of the surface temperature (Warnecke *et al.* 2016). This is likely due to the enhanced luminosity used in the current simulations. We also note that in the rotating cases the heat

flux is mostly radial near the equator, but more inclined with the rotation vector at high latitudes. This is a manifestation of latitudinal turbulent heat flux, which is often invoked to break the Taylor-Proudman balance in the Sun (e.g. [Brandenburg *et al.* 1992](#)). A poleward enthalpy flux has been reported in numerous earlier studies (e.g. [Pulkkinen *et al.* 1993](#), [Käpylä *et al.* 2011b](#), [Brun *et al.* 2017](#)).

The strong latitudinal variation of the depths of the various layers render latitudinal averaging of the radial coordinates of the transitions between different layers useless in these cases. In runs where an RZ develops (MHD3 and MHD4), the latitudinal variation of the depths of the different zones and of the enthalpy flux are significantly weaker, see Figure 2(f). However, for completeness, we list the latitudinally averaged coordinates of the bottoms of BZ, DZ, and OZ and the depths of the corresponding layers for all runs in Table 1. The values for runs RHDp, RHD1, RHD2, MHDp, MHD1, and MHD2, where strong latitudinal variations are seen, are listed in parentheses and should be considered as uncertain. We found that the DZ diminishes substantially in Runs MHD3 and MHD4 in comparison to the non-rotating case HD3 and HD4, whereas the depth of the OZ is influenced less. It is also noteworthy that in the rotating Kramers-based Runs RHD1 and MHD1, the overall velocities, measured by the Reynolds numbers, are higher than in the fixed profile runs RHDp and MHDp; see the second column of Table 1.

Our earlier Cartesian study indicated that the downflows are mostly responsible for the enthalpy flux in non-rotating overshooting convection (cf. Fig. 2 of [Käpylä *et al.* 2017b](#)). However, convective flows produce also a substantial (but downward) kinetic energy flux

$$\overline{F}_{\text{kin}} = \frac{1}{2} \overline{\rho \mathbf{u}^2 u_r}, \quad (26)$$

where $\mathbf{u} = \mathbf{U} - \overline{\mathbf{U}}$. Thus the total convected flux

$$\overline{F}_{\text{conv}} = \overline{F}_{\text{enth}} + \overline{F}_{\text{kin}}, \quad (27)$$

can be substantially different from the enthalpy flux. This is particularly true for the downflows, where the signs of the enthalpy and kinetic energy fluxes are opposite (cf. Fig. 1 of [Käpylä *et al.* 2017b](#)). An earlier study ([Cattaneo *et al.* 1991](#)) has suggested that the two contributions nearly cancel for the downflows. However, later studies of [Chan and Gigas \(1992\)](#) and [Brummell *et al.* \(2002\)](#) confirmed that cancellation occurs but the downflows contribute still approximately equally to the total energy transport. The main difference between the study of [Cattaneo *et al.* \(1991\)](#) and those of [Chan and Gigas \(1992\)](#) and [Brummell *et al.* \(2002\)](#) is that the latter include a stably stratified overshoot layer below the CZ, whereas in the former the whole domain is convectively unstable.

We study the detailed flux dynamics by separating the convective flux into kinetic and enthalpy fluxes from up- and downflows and represent them in terms of the corresponding luminosities:

$$\langle L_{\text{conv}} \rangle_{\theta\phi} = \langle L_{\text{enth}} \rangle_{\theta\phi} + \langle L_{\text{kin}} \rangle_{\theta\phi}, \quad (28)$$

$$\langle L_{\text{enth}} \rangle_{\theta\phi} = \langle L_{\text{enth}}^{\uparrow} \rangle_{\theta\phi} + \langle L_{\text{enth}}^{\downarrow} \rangle_{\theta\phi}, \quad (29)$$

$$\langle L_{\text{kin}} \rangle_{\theta\phi} = \langle L_{\text{kin}}^{\uparrow} \rangle_{\theta\phi} + \langle L_{\text{kin}}^{\downarrow} \rangle_{\theta\phi}. \quad (30)$$

Here \uparrow and \downarrow refer to contributions from up- and downflows, respectively, and $L_i = 4\pi r^2 F_i$ are the corresponding luminosities. Representative results are shown in Figure 3 from Runs HDp, HD4, MHD1, and MHD4. We find that significant cancellation of $\langle L_{\text{conv}}^{\downarrow} \rangle_{\theta\phi}$ occurs in all cases but that the downflows still contribute equally, or more, than the upflows to the total convected flux. This agrees with the Cartesian simulations of [Chan and Gigas \(1992\)](#), [Brummell *et al.* \(2002\)](#) and [Käpylä *et al.* \(2017b\)](#). No qualitative difference is seen between setups without and with stably stratified overshoot and radiative layers.

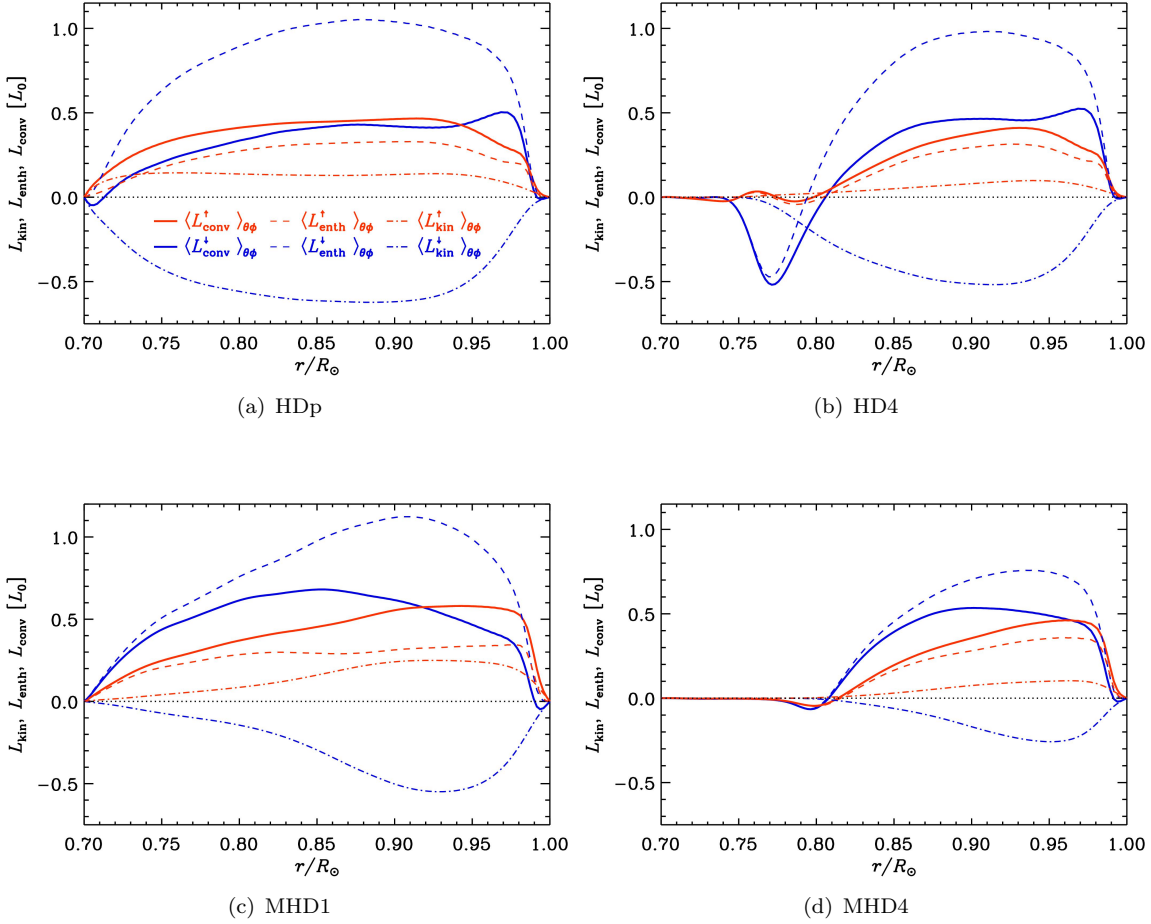


Figure 3. Convective (thick solid), enthalpy (dashed), and kinetic energy (dash-dotted) fluxes for upflows (red) and downflows (blue) from Runs HDp, HD4, MHD1, and MHD4.

3.2. Force balance

Recently, Käpylä *et al.* (2017b) and Hotta (2017) studied the force balance on up- and downflows in non-rotating Cartesian convection. A remarkable result from these studies is that the downflows appear to feel the Schwarzschild criterion, such that they are accelerated in unstable and decelerated in stable regions, while the upflows do not appear to do so. Here we study whether this result holds also in astrophysically more realistic setups that include rotation and magnetic fields in spherical coordinates.

We study this by measuring the the total force on the fluid

$$\mathcal{F}_r = \rho \frac{Du_r}{Dt}, \quad (31)$$

separately for the up- and downflows which are denoted by \uparrow and \downarrow , respectively. Representative results are shown in Figure 4 for the same set of runs as in Figure 3. Comparing the thick black-and-white and magenta curves in Figure 4(a) and (e), it is seen that for Run HDp the sign change of \mathcal{F}_r^\downarrow occurs roughly at the same average position as that of the radial entropy gradient. This appears to be the case also for \mathcal{F}_r^\uparrow at high latitudes and near the equator whereas at mid-latitudes \mathcal{F}_r^\uparrow is positive until roughly $r \approx 0.85R_\odot$. These results indicate that the downflows are accelerated in the Schwarzschild-unstable layer whereas the upflows accelerate mainly in the Schwarzschild-stable layer. This is clearly deviating from the behavior

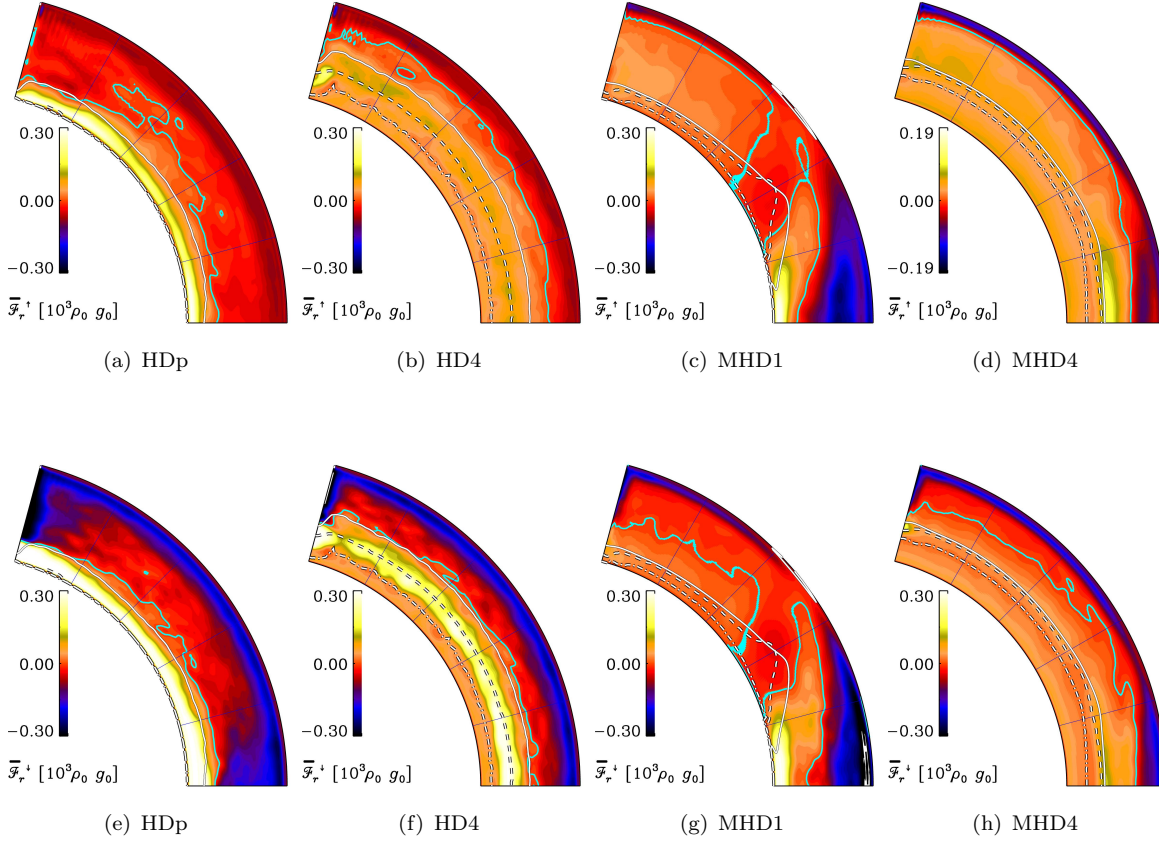


Figure 4. Total azimuthally radial force $\overline{\mathcal{F}}_r = \overline{\rho D u_r / Dt}$ on the upflows (upper row) and downflows (lower) for Runs HDp, HD4, MHD1, and MHD4. The thick green line indicates the zero level of the force.

of the Cartesian simulations with proper OZ and RZ, see Käpylä *et al.* (2017b) and Hotta (2017). However, in Run HD4, panels (b) and (f) of Figure 4, the results of the Cartesian simulations are again restored: the downflows appear to adhere to the Schwarzschild criterion and the upflows are accelerated in the lower part of the BZ.

The situation is significantly more complex in runs where rotation and magnetic fields are included. This is particularly clear in cases where the stably stratified layers are absent or very thin. This is seen, for example in Run MHD1 in Figure 4(c) and (g): at high latitudes, the upflows are accelerated everywhere except in a thin layer ($r \gtrsim 0.95R_\odot$) near the surface, whereas the downflows are accelerated roughly above $r \gtrsim 0.8R_\odot$. The upflows are, however, driven upward also in the stably stratified OZ and DZ. No clear relation to the Schwarzschild criterion can be identified. At mid-latitudes around the tangent cylinder, the total force is downward for both, up- and downflows. Outside the tangent cylinder, the force is very roughly following a radially decreasing trend as a function of cylindrical radius. For runs with more substantial OZ, such as MHD4 in Figure 4(d) and (h), the latitudinal variation is clearly weaker, and the force on the upflows appears to follow the Schwarzschild criterion in the deep parts in that the upflows are accelerated in the BZ and decelerated in the stably stratified DZ and OZ. The layer near the surface, where deceleration of the upflows occurs, is deeper near the equator also in these cases. The downflows, on the other hand, are decelerated in the lower part of the BZ well above the level where the Schwarzschild criterion indicates stability.

Although a detailed interpretation of the results is non-trivial, we can conclude that the presence of a substantial OZ has a significant influence on the large-scale dynamics of the system. These results are at odds with recent results of Hotta (2017) who used Cartesian

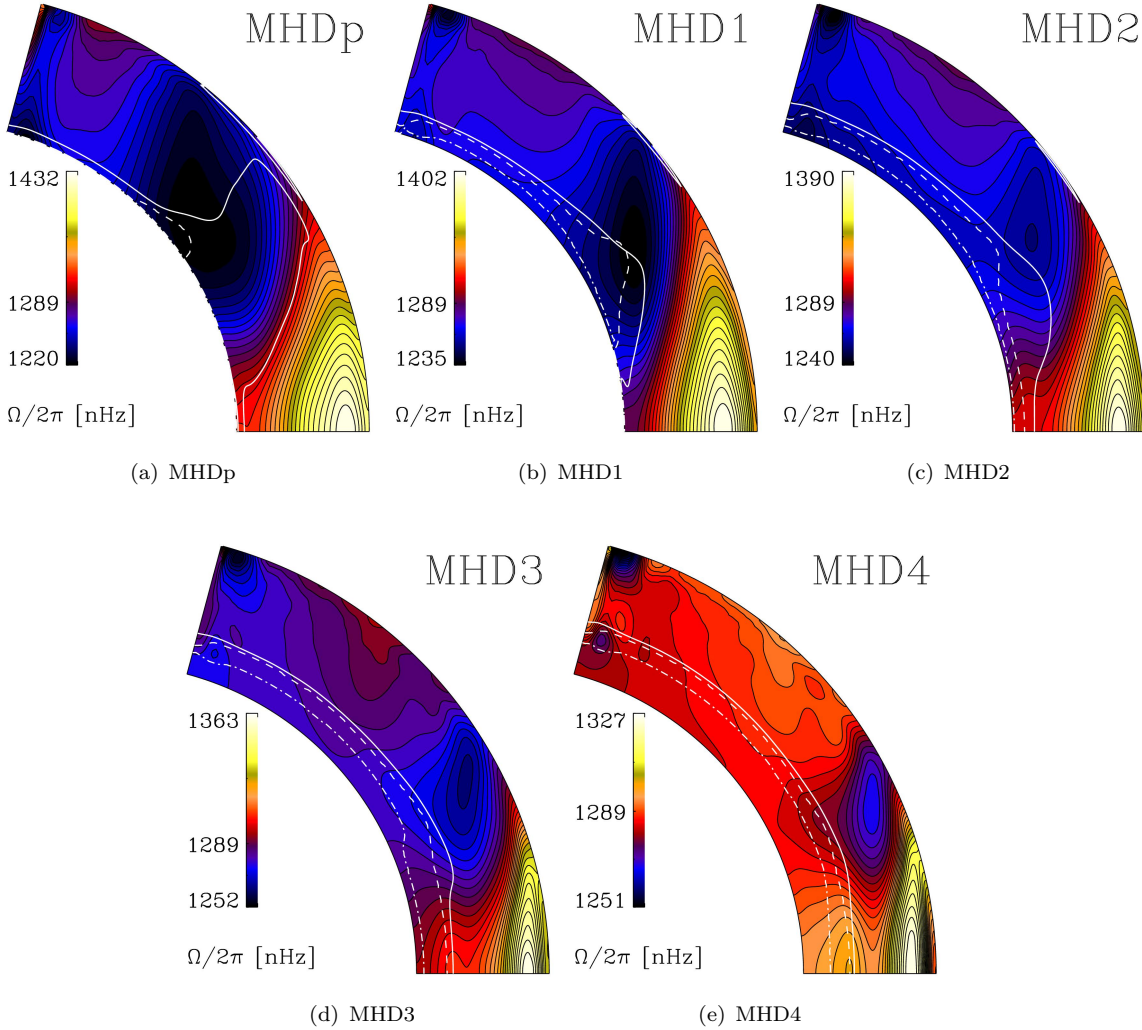


Figure 5. Time-averaged rotation profiles from the runs in the MHD set. The white solid, dashed, and dash-dotted lines indicate the bottoms of the buoyancy, Deardorff, and overshoot zones, respectively.

simulations to conclude that convective overshooting below the CZ of the Sun is only 0.4 per cent or 250 km, and that the interface between RZ and CZ could be well modeled by imposing suitable boundary conditions. Furthermore, global rotation also changes the behavior of the system qualitatively. However, the current study explores only a single rotation rate, leading to a rotationally constrained flow, at a modest supercriticality of convection. Studying the effects of rotation and higher Rayleigh numbers in more detail will be presented elsewhere.

3.3. Differential rotation and velocity spectra

Some mean-field models of solar differential rotation (Rempel 2005) have invoked a subadiabatic lower part of the CZ to break the Taylor-Proudman constraint which, in turn, manifests itself through cylindrical isocontours of constant angular velocity. Given the subadiabatic layers in the current simulations, it is of interest to study the rotation profiles in comparison to earlier studies. We show the time-averaged rotation profiles from the MHD runs in Figure 5.

We find that the isocontours of $\bar{\Omega} = \Omega_0 + \bar{U}_\phi/r \sin \theta$ are significantly tilted even in the run with a fixed heat conduction profile (MHDp). Furthermore, a mid-latitude minimum is

visible, but it is shallower, and occupies a wider latitude range than in previous simulations with similar rotation rates; see, e.g., Fig. 4 of [Augustson *et al.* \(2015\)](#) and Fig. 1 of [Warnecke \(2018\)](#). The mid-latitude minimum is most likely responsible for the equatorward migrating activity seen in the aforementioned studies. A near-surface shear layer is also clearly visible in the current runs. The most likely reason for the appearance of the latter is that the density stratification in the current runs is higher ($\Delta\rho \approx 60$) than in earlier studies with otherwise similar parameters (e.g. [Käpylä *et al.* 2012](#), [Warnecke *et al.* 2014](#), [Käpylä *et al.* 2017a](#)) where $\Delta\rho \approx 20$. This has also been found in recent simulations of [Matilsky \(2018\)](#). In theory, this allows the development of a near-surface layer where the rotational influence on the flow is weak, quantified by $\text{Co} < 1$. In such a parameter regime, the non-diffusive Reynolds stress, or Λ effect, responsible for the generation of differential rotation (e.g. [Rüdiger 1989](#)) reduces to a single term that drives a latitude-independent radial shear, as in [Barekat *et al.* \(2014\)](#), [Kitchatinov \(2016\)](#) and [Käpylä \(2018\)](#). However, the current results seem to confirm the results of [Robinson and Chan \(2001\)](#) in that extreme density stratification ([Hotta *et al.* 2015](#)) is not required for the appearance of a near-surface shear layer.

In Runs MHD1 and MHD2, the rotation profile is qualitatively similar to that in MHDp. The clearest difference is the enhanced radial gradient of $\bar{\Omega}$ near the surface at low latitudes. Also, the region of negative radial shear in mid-latitudes is enhanced—especially in the Deardorff layer in Run MHD2 (see the dashed and solid white lines in Figure 5). In the remaining runs (MHD3 and MHD4), the layer of negative radial shear is even more pronounced, but appears predominantly within the BZ. It is also apparent that the differential rotation creeps into the radiative interior due to the relatively high diffusivities used in the current simulations. The local minimum of $\bar{\Omega}$ at mid-latitudes, coinciding with the location of the tangent cylinder of the BZ to DZ transition near the equator, becomes more pronounced in Runs MHD3 and MHD4.

In recent studies, [Featherstone and Hindman \(2016a,b\)](#) investigated the effects of increasing supercriticality of convection and the rotational influence on the spectral energy distribution of convective flows in an effort to find clues to solve the convective conundrum. Furthermore, [Käpylä *et al.* \(2017b\)](#) found evidence that the structure of convective flows changes qualitatively when a smoothly varying heat conduction profile is used. Hence, next we study the effects of rotation, magnetic fields and stably stratified layers on the spectral energy distribution in spherical domains. To calculate the power spectra for the horizontal velocity, we follow the same procedure as in [Featherstone and Hindman \(2016a\)](#). For each run, we calculate the normalized power spectrum:

$$P_\ell = \frac{\sum_{m=-\ell}^{\ell} |u_{\ell,m}|^2}{\sum_{\ell} \sum_{m=-\ell}^{\ell} |u_{\ell,m}|^2}. \quad (32)$$

We separate the axisymmetric contribution, P_0 , given by the $m = 0$ mode to obtain the convective velocity spectra, P_{conv} , as the sum of the higher m modes.

Figure 6 shows the results for 4 representative runs. By looking at panels (a) and (b), it is clear that a prescribed profile for the heat conductivity (Run HDp) leads to higher energy in the large scales than in Run HD4 where substantial OZ and RZ are present. The fact that the power at large scales is dominated by the axisymmetric component is due to a strong coherent meridional flow that develops in the system. Similar large-scale convective modes have been reported in non-rotating and slowly rotating simulations in the past (e.g. [Brun and Palacios 2009](#), [Käpylä *et al.* 2018](#)). The difference in the spectra between Runs HDp and HD4 is that the large-scale flow in the latter is significantly weaker. On the other hand, by increasing the radiative diffusion in the rotating runs MHD1 and MHD4, see Figure 6(c) and (d), the total energy at large scales decreases by an order of magnitude and the peak in the non-axisymmetric spectra moves toward smaller scales. The lower power at large scales

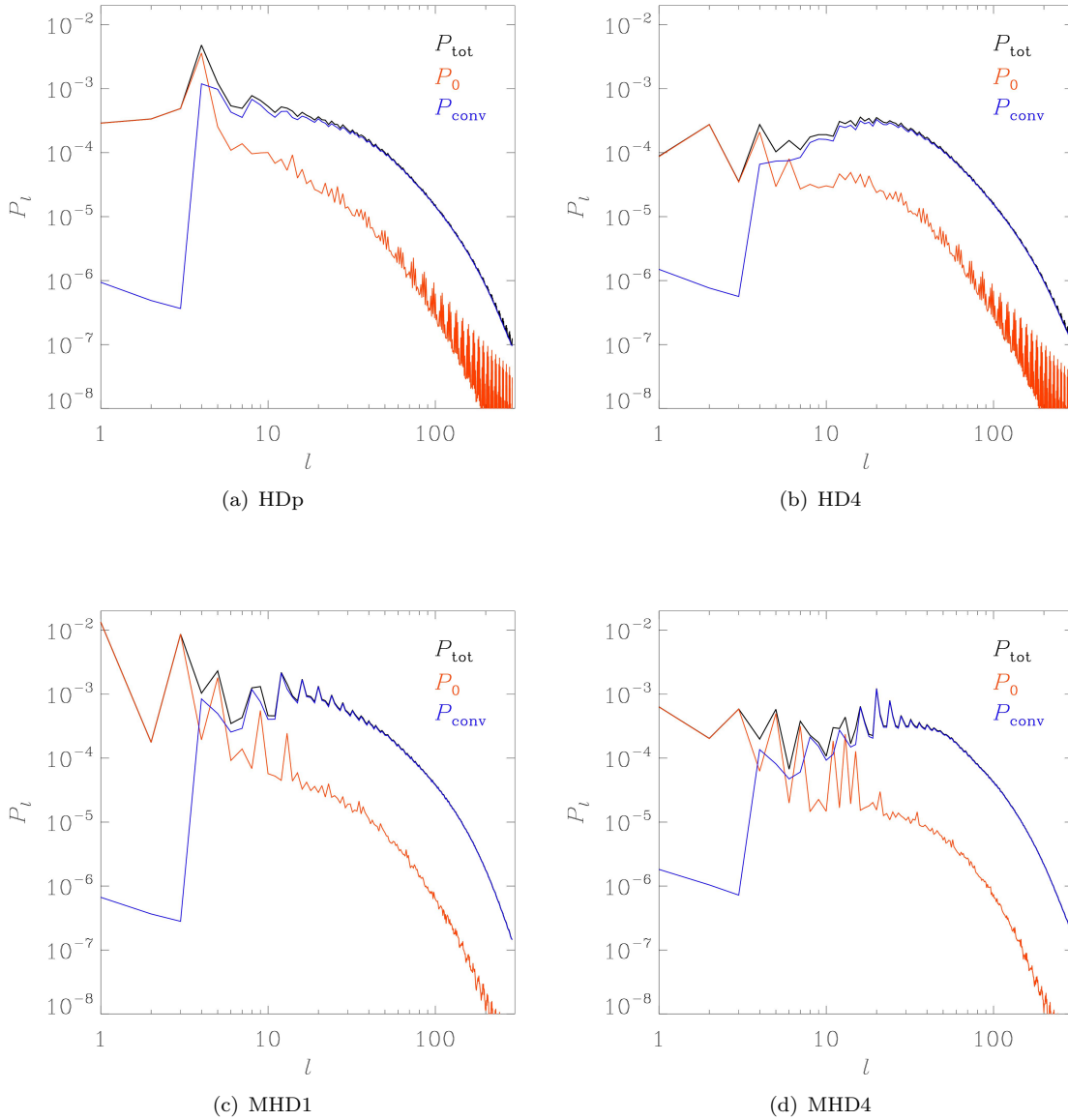


Figure 6. Power spectra of the total (black), axisymmetric (red), and non-axisymmetric (blue) parts of the velocity from runs (a) HDp, (b) HD1, (c) MHD1, and (d) MHD4.

is a consequence of weaker differential rotation, see Figure 5. The reason for the changing distribution of the non-axisymmetric power is not so easily distinguishable. The rotational influence on the flow is changing by roughly 20 per cent between Runs MHD1 and MHD4 (see the 3rd column of Table 1) and it is unlikely that this could have caused such a large effect. Another possibility is that some of the large-scale convective modes excited in Run MHD1 are absent in the shallower CZ of Run MHD4.

3.4. Dynamo solutions

We find that all of the current simulations show large-scale dynamo action. Time-latitude diagrams of the mean azimuthal field are shown in Figure 7. The solution in Run MHDp shows a cyclic large-scale field which, however, is relatively weak and stronger magnetic fields

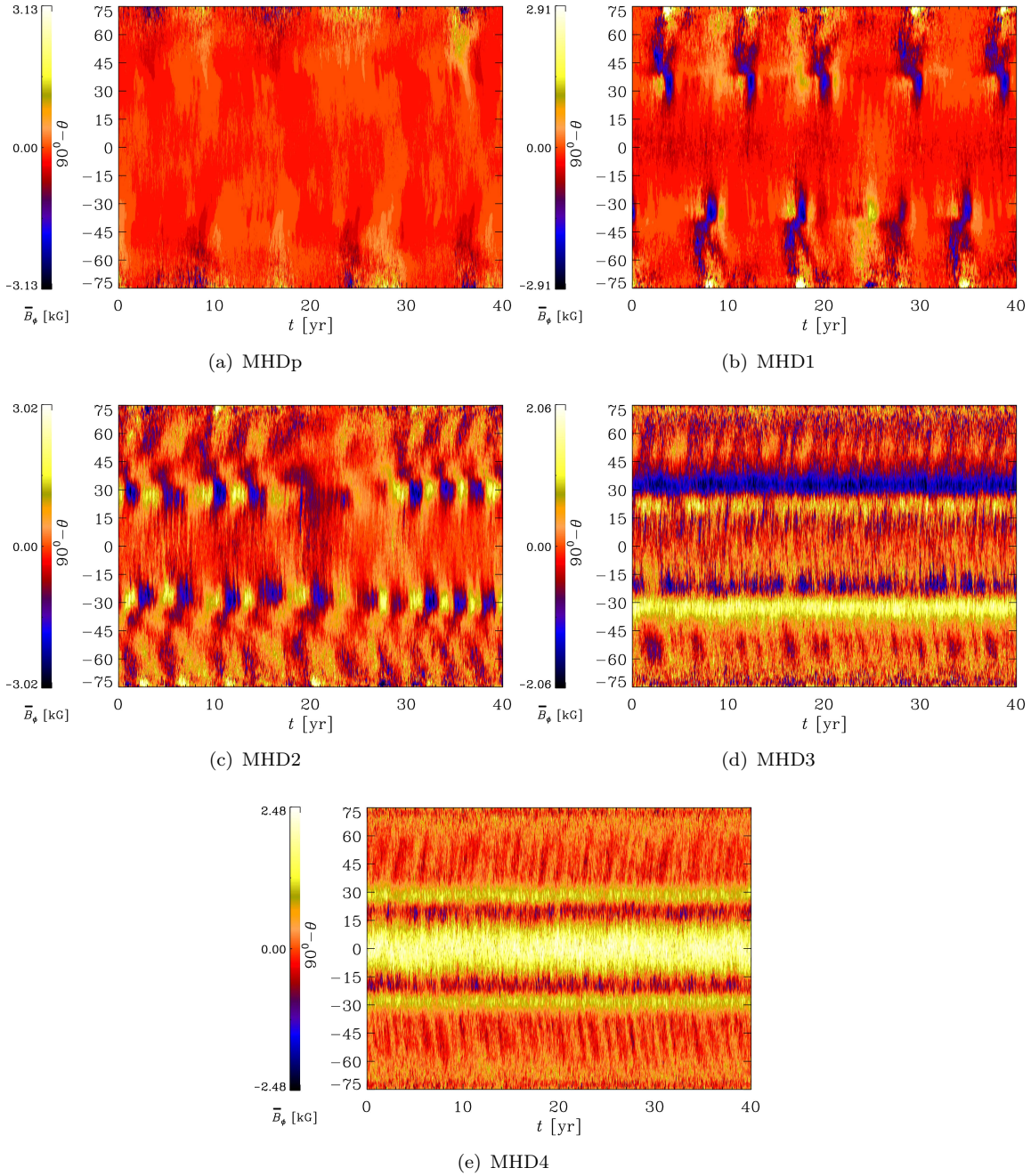


Figure 7. Azimuthally averaged azimuthal magnetic field \overline{B}_ϕ near the surface at $r/R_\odot = 0.98$ as a function of time from a 40 year time span from the runs in the MHD set.

are mostly concentrated toward high latitudes. In Run MHD1, the solution does not show clear polarity reversals, although a quasi-periodic component clearly appears; see Figure 7(b). This behavior is qualitatively similar to that reported in [Karak *et al.* \(2015\)](#) and in Run E2 of [Käpylä *et al.* \(2017a\)](#), which, apart from the lower density stratification, has otherwise similar parameters as the current Run MHD1.

In Run MHD2, a clearly oscillatory mode is excited, which is reminiscent of earlier results ([Käpylä *et al.* 2012, 2013](#), [Augustson *et al.* 2015](#), [Käpylä *et al.* 2016](#), [Warnecke 2018](#)). The main cycle period of a very similar run parameter-wise ([Käpylä *et al.* 2016](#)) was reported to be

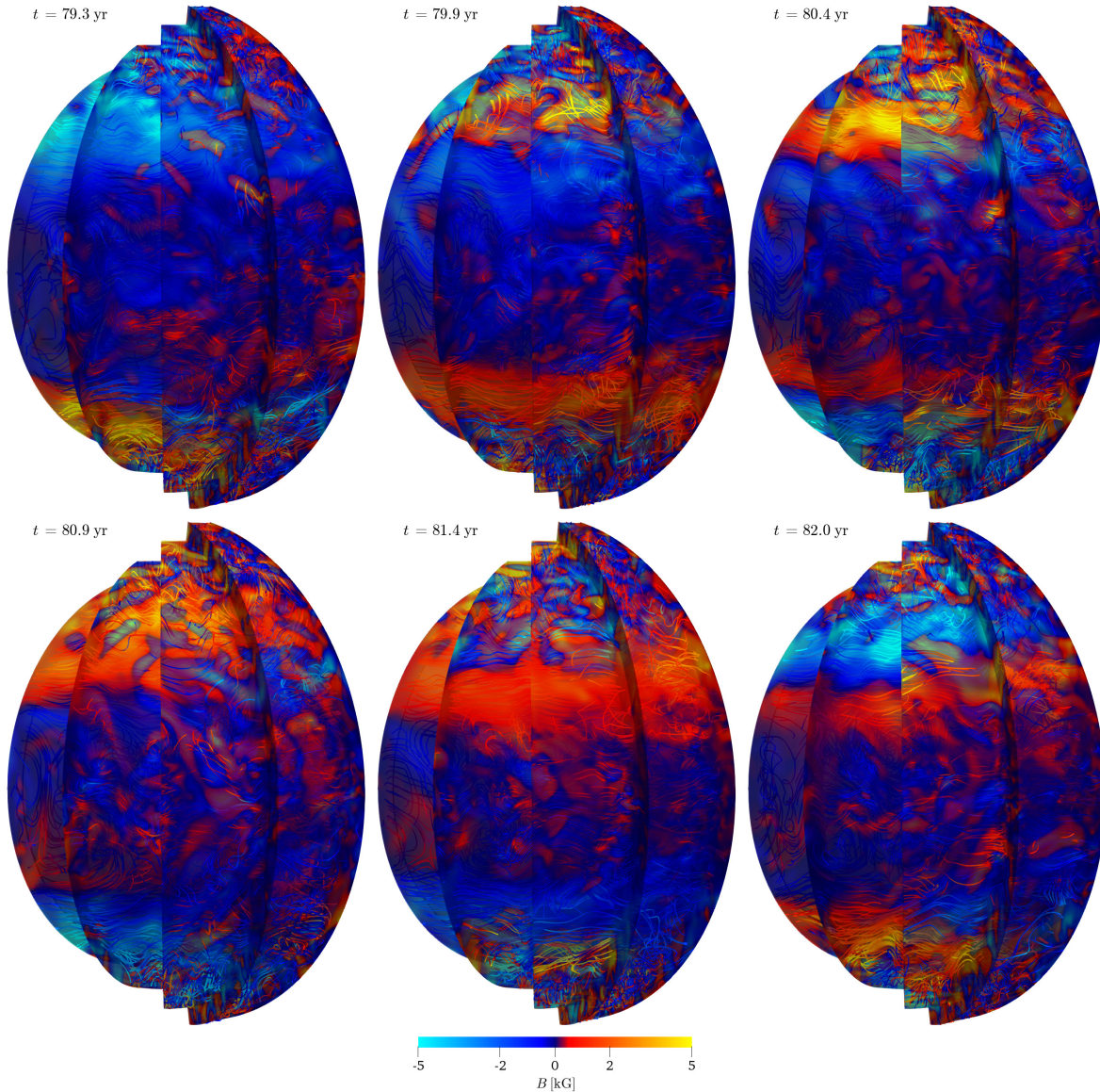


Figure 8. Magnetic fields lines and azimuthal magnetic field (colors) from six snapshots covering roughly one magnetic cycle from Run MHD2. The panels are separated by 0.5 – 0.6 years as indicated by the legends. The colour bar indicates the field strength in kilogauss.

roughly 5 years, whereas here the cycle is shorter nearly by a factor of two. Representations of the magnetic fields in different phases of the cycle are shown in Figure 8. Quantitative differences to Run MHD1 are relatively minor; the Reynolds and Coriolis numbers differ by roughly 10 per cent, see the 2nd and 3rd columns of Table 1. However, the Deardorff layer is thicker at low latitudes and the region of negative radial shear is wider at mid-latitudes in Run MHD2 in comparison to Run MHD1. The dynamo solution thus appears to be sensitive to relatively small changes in the flow properties. We also observe a quiescent period roughly between 15 and 25 years in physical time that can be interpreted as a Maunder minimum-type event (see also Augustson *et al.* 2015, Käpylä *et al.* 2016). During this event, also the dominant dynamo mode at the surface appears to change to a shorter one at late stages. The minimum event and the changing dynamo mode are due to a change of magnetic field structure in the deeper layers, where a mode with a possibly much longer cycle is dominating. This is in agreement with the conclusions of Käpylä *et al.* (2016).

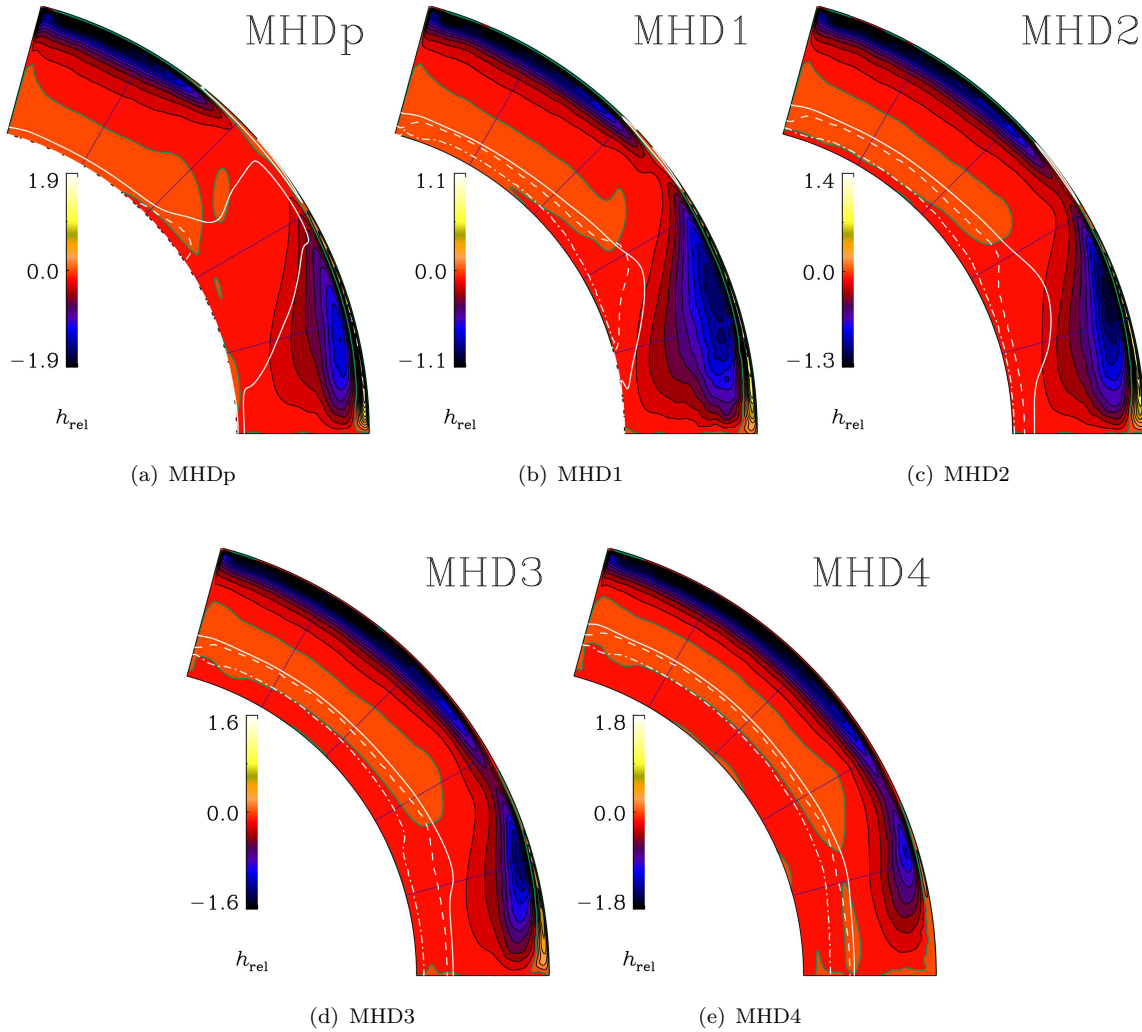


Figure 9. Time-averaged relative kinetic helicity from the MHD runs.

In the two remaining simulations (MHD3 and MHD4), the dynamo switches to a non-oscillatory mode. In these cases the surface appearance reflects the occurrence of a large-scale field stored beneath the CZ in the stably stratified layers. The behavior seen in the current simulations is not likely to occur to the same extent in real stars where the small magnetic diffusivity will not allow the magnetic fields to penetrate the radiative layers below the CZ.

Given that the dominant dynamo mode changes as a function of depth of the stably stratified layers below the CZ, it is of interest to study the diagnostics that are commonly held responsible for the generation of large-scale magnetic fields and cycles. One such diagnostic is the kinetic helicity of the flow, which can, for high conductivity, be associated with the α effect of mean-field electrodynamics (Steenbeck *et al.* 1966, Krause and Rädler 1980). Furthermore, it has been shown by numerical simulations that the sign of the kinetic helicity can change under certain conditions in the deep parts of the convection zone and lead to a change of the propagation direction of the dynamo wave (Duarte *et al.* 2016). Such reversals of the resulting α effect have been utilized in mean-field dynamo theory starting with the work of Yoshimura (1972).

Figure 9 shows time-averaged relative kinetic helicity $h_{\text{rel}} = \overline{\mathbf{u} \cdot \boldsymbol{\omega}} / u_{\text{rms}} \omega_{\text{rms}}$ from the MHD runs. Here, $\boldsymbol{\omega} = \nabla \times \mathbf{u}$ is the vorticity of the fluctuating velocity. We do find a region of

inverted helicity at the base of the CZ in all runs. However, this region is concentrated at high latitudes in Runs MHDp and MHD1–2. Although the region of positive helicity extends to lower latitudes in Runs MHD3 and MHD4, it is still confined within the tangent cylinder with respect to the bottom of the BZ. Only in Run MHD4, a clear inversion is seen at low latitudes near the equator.

4. Conclusions

In the current study we have presented the first simulations of convection in rotating spherical coordinates with a heat conduction prescription based on the Kramers opacity law in a dynamical fashion such that the depth of the CZ is not fixed a priori. We have demonstrated that in such setups, the depth of the CZ is controlled by the overall efficiency of the convective energy transport. Enhancing the radiative energy transport reduces the fraction of energy transported by convection in the deep parts, and is associated with the appearance of stably stratified Deardorff, overshoot, and radiative layers below the Schwarzschild-unstable layer. The enhanced luminosity in the current simulations allows the models to be evolved to a thermally saturated state in a reasonable time and we do not have to resort to changing the heat conductivity in the convectively stable layers (e.g. Brun *et al.* 2017, Hotta 2017). We have shown that the presence of such a stable layer has several interesting implications for the dynamics of convection.

Although the up- and downflows contribute roughly equally to the energy transport in all of the cases studied here, the presence of stably stratified overshoot and radiative layers are reflected in the force balance. This suggests fundamentally different dynamics in systems with and without such layers. In the rotating cases with $\Omega_0 = 3\Omega_\odot$ and without significant stably stratified layers, the convective energy transport is highly anisotropic with mid-latitude regions producing an almost negligible contribution to the overall luminosity. If, on the other hand, stably stratified layers are present, the latitudinal dependence of convective energy transport is much weaker.

The changes in the rotation profiles and large-scale magnetism are more subtle and the interpretation is less straightforward. However, the current simulations show clearly a near-surface shear layer at low latitudes—irrespective of the prescription of radiative diffusion. This is possibly due to the somewhat higher density stratification in the current simulations in comparison to several previous studies. The appearance of stably stratified layers at the bottom of the domain tends to produce a layer of negative radial shear at the base of the CZ. However, this leads to clearly equatorward migrating large-scale magnetic fields only in a single case. Although an inversion of the kinetic helicity is observed in the OZ and the lower part of the CZ in our cases with the shallowest convection zone, they exhibit quasi-stationary large-scale magnetic fields.

References

- Augustson, K., Brun, A.S., Miesch, M. and Toomre, J., Grand Minima and Equatorward Propagation in a Cycling Stellar Convective Dynamo. *Astrophys. J.*, 2015, **809**, 149.
 Barekat, A. and Brandenburg, A., Near-polytropic stellar simulations with a radiative surface. *Astron. Astrophys.*, 2014, **571**, A68.
 Barekat, A., Schou, J. and Gizon, L., The radial gradient of the near-surface shear layer of the Sun. *Astron. Astrophys.*, 2014, **570**, L12.

- Bekki, Y., Hotta, H. and Yokoyama, T., Convective Velocity Suppression via the Enhancement of the Subadiabatic Layer: Role of the Effective Prandtl Number. *Astrophys. J.*, 2017, **851**, 74.
- Brandenburg, A., Stellar Mixing Length Theory with Entropy Rain. *Astrophys. J.*, 2016, **832**, 6.
- Brandenburg, A., Moss, D. and Tuominen, I., Stratification and thermodynamics in mean-field dynamos. *Astron. Astrophys.*, 1992, **265**, 328–344.
- Brandenburg, A., Nordlund, A. and Stein, R.F., Astrophysical convection and dynamos; in *Geophysical and Astrophysical Convection, Contributions from a workshop sponsored by the Geophysical Turbulence Program at the National Center for Atmospheric Research, October, 1995*. Edited by Peter A. Fox and Robert M. Kerr. Published by Gordon and Breach Science Publishers, The Netherlands, 2000, p. 85–105, edited by P.A. Fox and R.M. Kerr, Aug., 2000, pp. 85–105.
- Browning, M.K., Miesch, M.S., Brun, A.S. and Toomre, J., Dynamo Action in the Solar Convection Zone and Tachocline: Pumping and Organization of Toroidal Fields. *Astrophys. J. Lett.*, 2006, **648**, L157–L160.
- Brummell, N.H., Clune, T.L. and Toomre, J., Penetration and Overshooting in Turbulent Compressible Convection. *Astrophys. J.*, 2002, **570**, 825–854.
- Brun, A.S. and Browning, M.K., Magnetism, dynamo action and the solar-stellar connection. *Liv. Rev. Sol. Phys.*, 2017, **14**, 4.
- Brun, A.S. and Palacios, A., Numerical Simulations of a Rotating Red Giant Star. I. Three-dimensional Models of Turbulent Convection and Associated Mean Flows. *Astrophys. J.*, 2009, **702**, 1078–1097.
- Brun, A.S., Strugarek, A., Varela, J., Matt, S.P., Augustson, K.C., Emeriau, C., DoCao, O.L., Brown, B. and Toomre, J., On Differential Rotation and Overshooting in Solar-like Stars. *Astrophys. J.*, 2017, **836**, 192.
- Brun, A.S. and Toomre, J., Turbulent Convection under the Influence of Rotation: Sustaining a Strong Differential Rotation. *Astrophys. J.*, 2002, **570**, 865–885.
- Busse, F.H., Differential Rotation in Stellar Convection Zones. *Astrophys. J.*, 1970, **159**, 629.
- Cattaneo, F., Brummell, N.H., Toomre, J., Malagoli, A. and Hurlburt, N.E., Turbulent compressible convection. *Astrophys. J.*, 1991, **370**, 282–294.
- Chan, K.L. and Gigas, D., Downflows and entropy gradient reversal in deep convection. *Astrophys. J. Lett.*, 1992, **389**, L87–L90.
- Cossette, J.F. and Rast, M.P., Supergranulation as the Largest Buoyantly Driven Convective Scale of the Sun. *Astrophys. J. Lett.*, 2016, **829**, L17.
- Deardorff, J.W., The Counter-Gradient Heat Flux in the Lower Atmosphere and in the Laboratory.. *J. Atmosph. Sci.*, 1966, **23**, 503–506.
- Deluca, E.E. and Gilman, P.A., Dynamo theory for the interface between the convection zone and the radiative interior of a star: Part I model equations and exact solutions. *Geophysical and Astrophysical Fluid Dynamics*, 1986, **37**, 85–127.
- Dikpati, M. and Charbonneau, P., A Babcock-Leighton Flux Transport Dynamo with Solar-like Differential Rotation. *Astrophys. J.*, 1999, **518**, 508–520.
- Duarte, L.D.V., Wicht, J., Browning, M.K. and Gastine, T., Helicity inversion in spherical convection as a means for equatorward dynamo wave propagation. *Monthly Notices of the Roy. Astron. Soc.*, 2016, **456**, 1708–1722.
- Featherstone, N.A. and Hindman, B.W., The Emergence of Solar Supergranulation as a Natural Consequence of Rotationally Constrained Interior Convection. *Astrophys. J. Lett.*, 2016a, **830**, L15.
- Featherstone, N.A. and Hindman, B.W., The Spectral Amplitude of Stellar Convection and Its Scaling in the High-Rayleigh-number Regime. *Astrophys. J.*, 2016b, **818**, 32.
- Gastine, T., Yadav, R.K., Morin, J., Reiners, A. and Wicht, J., From solar-like to antisolar differential rotation in cool stars. *Monthly Notices of the Roy. Astron. Soc.*, 2014, **438**, L76–L80.
- Ghizaru, M., Charbonneau, P. and Smolarkiewicz, P.K., Magnetic Cycles in Global Large-eddy Simulations of Solar Convection. *Astrophys. J. Lett.*, 2010, **715**, L133–L137.
- Gilman, P.A., Nonlinear Dynamics of Boussinesq Convection in a Deep Rotating Spherical Shell. I. *Geophys. Astrophys. Fluid Dynam.*, 1977, **8**, 93–135.
- Gilman, P.A. and Miller, J., Nonlinear convection of a compressible fluid in a rotating spherical shell. *Astrophys. J. Suppl.*, 1986, **61**, 585–608.
- Gizon, L. and Birch, A.C., Helioseismology challenges models of solar convection. *Proc. Nat. Acad. Sci.*, 2012, **109**, 11896–11897.
- Hanasoge, S.M., Duvall, T.L. and Sreenivasan, K.R., Anomalously weak solar convection. *Proc. Natl. Acad. Sci.*, 2012, **109**, 11928–11932.
- Hotta, H., Solar Overshoot Region and Small-scale Dynamo with Realistic Energy Flux. *Astrophys. J.*, 2017, **843**, 52.
- Hotta, H., Rempel, M. and Yokoyama, T., High-resolution Calculation of the Solar Global Convection with the Reduced Speed of Sound Technique. II. Near Surface Shear Layer with the Rotation. *Astrophys. J.*, 2015, **798**, 51.
- Hurlburt, N.E., Toomre, J. and Massaguer, J.M., Two-dimensional compressible convection extending over multiple scale heights. *Astrophys. J.*, 1984, **282**, 557–573.
- Käpylä, M.J., Käpylä, P.J., Olsper, N., Brandenburg, A., Warnecke, J., Karak, B.B. and Pelt, J., Multiple dynamo modes as a mechanism for long-term solar activity variations. *Astron. Astrophys.*, 2016, **589**, A56.
- Käpylä, P.J., Magnetic and rotational quenching of the Λ effect. *arXiv:1712.08045*, 2018.
- Käpylä, P.J., Käpylä, M.J. and Brandenburg, A., Confirmation of bistable stellar differential rotation profiles.

- Astron. Astrophys.*, 2014, **570**, A43.
- Käpylä, P.J., Käpylä, M.J. and Brandenburg, A., Small-scale dynamos in simulations of stratified turbulent convection. *arXiv:1802.09607*, 2018.
- Käpylä, P.J., Käpylä, M.J., Olsper, N., Warnecke, J. and Brandenburg, A., Convection-driven spherical shell dynamos at varying Prandtl numbers. *Astron. Astrophys.*, 2017a, **599**, A4.
- Käpylä, P.J., Korpi, M.J., Brandenburg, A., Mitra, D. and Tavakol, R., Convective dynamos in spherical wedge geometry. *Astron. Nachr.*, 2010, **331**, 73.
- Käpylä, P.J., Mantere, M.J. and Brandenburg, A., Effects of stratification in spherical shell convection. *Astron. Nachr.*, 2011a, **332**, 883.
- Käpylä, P.J., Mantere, M.J. and Brandenburg, A., Cyclic Magnetic Activity due to Turbulent Convection in Spherical Wedge Geometry. *Astrophys. J. Lett.*, 2012, **755**, L22.
- Käpylä, P.J., Mantere, M.J., Cole, E., Warnecke, J. and Brandenburg, A., Effects of Enhanced Stratification on Equatorward Dynamo Wave Propagation. *Astrophys. J.*, 2013, **778**, 41.
- Käpylä, P.J., Mantere, M.J., Guerrero, G., Brandenburg, A. and Chatterjee, P., Reynolds stress and heat flux in spherical shell convection. *Astron. Astrophys.*, 2011b, **531**, A162.
- Käpylä, P.J., Rheinhardt, M., Brandenburg, A., Arlt, R., Käpylä, M.J., Lagg, A., Olsper, N. and Warnecke, J., Extended Subadiabatic Layer in Simulations of Overshooting Convection. *Astrophys. J. Lett.*, 2017b, **845**, L23.
- Karak, B.B., Käpylä, P.J., Käpylä, M.J., Brandenburg, A., Olsper, N. and Pelt, J., Magnetically controlled stellar differential rotation near the transition from solar to anti-solar profiles. *Astron. Astrophys.*, 2015, **576**, A26.
- Karak, B.B., Miesch, M. and Bekki, Y., Consequences of high effective Prandtl number on solar differential rotation and convective velocity. *arXiv:1801.00560*, 2018.
- Kitchatinov, L.L., Rotational shear near the solar surface as a probe for subphotospheric magnetic fields. *Astron. Lett.*, 2016, **42**, 339–345.
- Krause, F. and Rädler, K.H., *Mean-field Magnetohydrodynamics and Dynamo Theory*, 1980 (Oxford: Pergamon Press).
- Matilsky, L., Toward a Self-Consistent Dynamical Model of the NSSL; in *American Astronomical Society Meeting Abstracts*, Vol. 231 of *American Astronomical Society Meeting Abstracts*, Jan., 2018, p. 315.03.
- Miesch, M.S., Brun, A.S. and Toomre, J., Solar Differential Rotation Influenced by Latitudinal Entropy Variations in the Tachocline. *Astrophys. J.*, 2006, **641**, 618–625.
- Miesch, M.S. and Toomre, J., Turbulence, Magnetism, and Shear in Stellar Interiors. *Ann. Rev. Fluid Mech.*, 2009, **41**, 317–345.
- Mitra, D., Tavakol, R., Brandenburg, A. and Moss, D., Turbulent Dynamos in Spherical Shell Segments of Varying Geometrical Extent. *Astrophys. J.*, 2009, **697**, 923–933.
- O’Mara, B., Miesch, M.S., Featherstone, N.A. and Augustson, K.C., Velocity amplitudes in global convection simulations: The role of the Prandtl number and near-surface driving. *Adv. Space Res.*, 2016, **58**, 1475–1489.
- Parker, E.N., The dynamo dilemma. *Solar Phys.*, 1987, **110**, 11–21.
- Passos, D. and Charbonneau, P., Characteristics of magnetic solar-like cycles in a 3D MHD simulation of solar convection. *Astron. Astrophys.*, 2014, **568**, A113.
- Pulkkinen, P., Tuominen, I., Brandenburg, A., Nordlund, A. and Stein, R.F., Rotational effects on convection simulated at different latitudes. *Astron. Astrophys.*, 1993, **267**, 265–274.
- Rempel, M., Solar Differential Rotation and Meridional Flow: The Role of a Subadiabatic Tachocline for the Taylor-Proudman Balance. *Astrophys. J.*, 2005, **622**, 1320–1332.
- Robinson, F.J. and Chan, K.L., A large-eddy simulation of turbulent compressible convection: differential rotation in the solar convection zone. *Monthly Notices of the Roy. Astron. Soc.*, 2001, **321**, 723–732.
- Rüdiger, G., *Differential Rotation and Stellar Convection. Sun and Solar-type Stars*, 1989 (Berlin: Akademie Verlag).
- Schou, J., Antia, H.M., Basu, S., Bogart, R.S., Bush, R.I., Chitre, S.M., Christensen-Dalsgaard, J., di Mauro, M.P., Dziembowski, W.A., Eff-Darwich, A., Gough, D.O., Haber, D.A., Hoeksema, J.T., Howe, R., Korzenik, S.G., Kosovichev, A.G., Larsen, R.M., Pijpers, F.P., Scherrer, P.H., Sekii, T., Tarbell, T.D., Title, A.M., Thompson, M.J. and Toomre, J., Helioseismic Studies of Differential Rotation in the Solar Envelope by the Solar Oscillations Investigation Using the Michelson Doppler Imager. *Astrophys. J.*, 1998, **505**, 390–417.
- Spruit, H., Convection in stellar envelopes: a changing paradigm. *Mem. d. Soc. Astron. It.*, 1997, **68**, 397.
- Steenbeck, M., Krause, F. and Rädler, K.H., Berechnung der mittleren Lorentz-Feldstärke $\mathbf{v} \times \mathbf{B}$ für ein elektrisch leitendes Medium in turbulenter, durch Coriolis-Kräfte beeinflusster Bewegung. *Zeitschrift Naturforschung Teil A*, 1966, **21**, 369.
- Vitense, E., Die Wasserstoffkonvektionszone der Sonne. Mit 11 Textabbildungen. *Z. Astrophys.*, 1953, **32**, 135.
- Warnecke, J., Dynamo cycles in global convection simulations of solar-like stars. *arXiv:1712.01248*, 2018.
- Warnecke, J., Käpylä, P.J., Käpylä, M.J. and Brandenburg, A., On The Cause of Solar-like Equatorward Migration in Global Convective Dynamo Simulations. *Astrophys. J. Lett.*, 2014, **796**, L12.
- Warnecke, J., Käpylä, P.J., Käpylä, M.J. and Brandenburg, A., Influence of a coronal envelope as a free boundary to global convective dynamo simulations. *Astron. Astrophys.*, 2016, **596**, A115.
- Weiss, A., Hillebrandt, W., Thomas, H.C. and Ritter, H., *Cox and Giuli’s Principles of Stellar Structure*, 2004 (Cambridge, UK: Cambridge Scientific Publishers Ltd).
- Yoshimura, H., On the Dynamo Action of the Global Convection in the Solar Convection Zone. *Astrophys. J.*,

- 1972, **178**, 863–886.
Zahn, J.P., Convective penetration in stellar interiors. *Astron. Astrophys.*, 1991, **252**, 179–188.